Resonant Excitation of Surface Plasmon for Wakefield Acceleration by Beating GW Lasers on Smooth Cylindrical Surface

Bifeng Lei,[1,2,*] Hao Zhang,[1,2] Alexandre Bonatto,[3] Bin Liu,[4] Javier Resta-López,[5,6] Matt Zepf,[7,8] Guoxing Xia,[9,2] and Carsten Welsch[1,2]

[1]*Department of Physics, The University of Liverpool, Liverpool, L69 3BX, United Kingdom*
[2]*Cockcroft Institute, Warrington WA4 4AD, United Kingdom*
[3]*Federal University of Health Sciences of Porto Alegre, Porto Alegre, Rio Grande do Sul, 90050-170, Brazil*
[4]*Guangdong Institute of Laser Plasma Accelerator Technology, Guangzhou, 510415, China*
[5]*ICMUV, Universidad de Valencia, 46071 Valencia, Spain*
[6]*Department of Applied Physics and Electromagnetism, Universidad de Valencia, Burjassot, 46100, Spain*
[7]*Helmholtz Institute Jena, Fröbelstieg 3, 07743 Jena, Germany*
[8]*Faculty of Physics and Astronomy, Friedrich-Schiller-Universität Jena, 07743 Jena, Germany*
[9]*Department of Physics and Astronomy, The University of Manchester, Manchester M13 9PL, United Kingdom*

(Received 16 February 2026; accepted 6 August 2026; published 4 September 2026)

We present a theoretical and numerical study of resonant surface-plasmon (SP) excitation driven by the beating of two copropagating laser pulses on a smooth cylindrical plasma-vacuum interface. Analytical formulas for the SP dispersion relation, field amplitude, geometric coupling factor, and resonance conditions are derived and validated by fully three-dimensional particle-in-cell simulations. We show that the curvature-modified SP dispersion enables the optical beat wave to resonantly drive an axial SP wakefield that leaks into the vacuum channel. This enables a grating-free surface-plasmon phase-matching mechanism, which is not available on a smooth planar interface. Under matched resonance conditions, few-gigawatt (GW) lasers can drive tens of GV/m SP wakefields and initiate electron trapping, while tens to hundreds of GW drivers can reach sub-TV/m fields. It therefore opens a low-power, grating-free route toward portable laser-driven surface plasma wakefield accelerators.

DOI: 10.1103/2dkn-db5z

Surface plasmons (SPs) are collective electron oscillations localized at the interface between a conductor and an insulator [1]. In conventional configurations, SP excitation requires momentum-matching techniques to bridge the mismatch between photon and plasmon wave vectors [2–4], which becomes increasingly restrictive for high-intensity drivers and limits operational flexibility.

Recent progress in high-power laser-driven grating-free surface plasmons on a smooth surface has opened a new route toward ultrahigh gradient, ultracompact plasma-based particle acceleration and radiation generation [5–9]. In these approaches, SPs are excited when the in-plane translational symmetry is broken during a laser pulse scattering with a smooth surface of a finite edge [10] or curvature. The efficiency depends primarily on the mode overlap between the incident laser field and the SP eigenfield. Because the surface can strongly shape eigenmodes, it enables the geometry-controlled SP coupling with the precise mode manipulation. Cylindrical surfaces, such as the inner wall of a microtube, in particular, have been shown to offer unique opportunities for SP-based wakefield acceleration of both electron and positron beams [9]. This method is significantly distinct from near-surface electron surfing on planar grating targets [11]. In the highly nonlinear regime, SPs can, in principle, sustain a bubble wakefield of amplitude approaching hundreds of TV/m with self-injection by using a solid microtarget [12–14]. While solid-density media have a long history in compact wakefield acceleration [15,16], carbon nanotube targets are recently proposed not only to offer favorable thermal and electrical properties for efficient smooth-surface-bounded SP excitation, but also to provide substantial flexibility in achievable plasma density, spanning 10^{19}–10^{24} cm^{-3} [17], which enables the low-density surface plasma as platform [18].

However, these concepts typically rely on either high-density relativistic beams or high-power lasers operating in the hundreds of terawatts to petawatts range as drivers, which remain costly and bulky for many laboratories, and are poorly suited to applications where flexibility and

*Contact author: bifeng.lei@liverpool.ac.uk

portability are important. Moreover, target survivability under strong electromagnetic fields of high-power lasers often constrains operation in an effectively single-shot mode, severely limiting the repetition rate. Low-power lasers can be more compact, economical and comparatively target-friendly, such as fiber lasers, which can deliver up to 5 GW) power on target [19]. This power is generally insufficient to directly drive a wakefield of amplitude high enough for electron self-injection and acceleration inside the gaseous bulk plasma [20]. Beating of two laser frequencies can resonantly drive bulk plasma waves for enhanced electron acceleration [21,22] and SP on a magnetized planar surface for THz generation [23] that can substantially reduce the requirement on the power of lasers. However, the use of beating waves to resonantly drive SP-based wakefield on a smooth cylindrical surface for relativistic particle acceleration has not yet been considered, while this promises a new route toward low-power laser-driven plasma-based acceleration with great flexibility.

In this Letter, we demonstrate that SP-based wakefields with amplitudes up to a few TV/m can be resonantly generated by the beating of two GW-level laser pulses on a smooth cylindrical microtube surface, thereby enabling electron self-trapping and acceleration. We develop a self-consistent theoretical framework and give analytical formulas for the SP dispersion relation, field amplitude, geometric coupling factor, and resonance conditions, which are quantitatively validated by fully 3D particle-in-cell (PIC) simulations. We show that curvature-induced geometric effects substantially modify the SP dispersion and thereby enable resonant phase matching with laser beat waves. This phase-matching mechanism is not available on a smooth planar interface under the same copropagating optical beat-wave conditions. Under matched resonance conditions, the amplitude of SP-based wakefields can be significantly amplified. Our results further indicate that laser powers of only a few GW are sufficient to generate SP fields at the tens of GV/m level, identifying fiber lasers as practical drivers. This Letter thus opens a pathway toward microscale electron accelerators for portable applications, such as endoscopic sources [24].

Beat-wave-driven SP excitation on a smooth cylindrical surface can be demonstrated by a fully 3D PIC simulation done by WarpX [25] as shown in Fig. 1. Two laser pulses of wavelengths $\lambda_1 = 0.8$ μm and $\lambda_2 = 0.64$ μm copropagate inside a microtube of a vacuum channel radius $a = 1.5$ μm. The normalised laser strength $a_{0,1} = a_{0,2} = 0.8$ and the rms pulse durations are the same, $\tau_L = 50$ fs, which satisfies $\omega_1 \tau_L \gg 1$, $\omega_2 \tau_L \gg 1$, and $\Delta\omega \tau_L \gg 1$ with beating frequency $\Delta\omega = |\omega_1 - \omega_2|$ and laser frequencies $\omega_1 = 2\pi c/\lambda_1$ and $\omega_2 = 2\pi c/\lambda_2$. A cycle-averaged ponderomotive description is therefore valid. These parameters give the laser peak power of approximately 200 and 320 GW, respectively. The carbon atom density is 1×10^{20} cm^{-3},

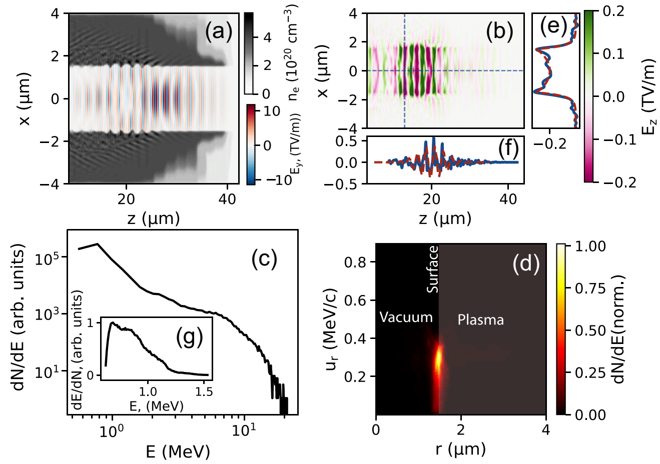

FIG. 1. PIC results after two laser pulses copropagating 40 μm inside a solid microtube: (a) electron density (gray) and beating laser field E_y (blue-red) in xz plane. (b) Acceleration field E_z in xz plane. (c) Energy spectrum of the electron beam accelerated. (d) Radial phase space (r, u_r) of the accelerated electron beam. The vacuum and plasma regimes are on the left and right, respectively. Blue solid lines in panels (e) and (f) show cuts—at the dashed lines depicted in panel (b)—of the transverse ($z \simeq 17$ μm) and longitudinal (on axis, $x = 0$ μm) E_z. Red dashed lines are from analytical calculation. (g) Energy spectrum of the electron beam accelerated inside the vacuum channel.

which can be structured by vertically aligned carbon nanotube (VCNT) forest with a tube density of 1×10^{11} tube/cm^2 giving the free electron density about 4×10^{20} cm^{-3}, as such laser pulses can fully ionize the σ bond of the carbon atom. The ionization energies are modified with the carbon nanotube properties in simulations. The laser spot size is $w_0 = 3.0$ μm, which gives 60% of on-wall intensity. The simulation window is $8 \times 8 \times 40$ μm with $192 \times 192 \times 768$ cells in x, y, and z directions, respectively. There are $2 \times 2 \times 2$ microparticles in each cell. Two vacuum sections of 20 μm are placed longitudinally at the head and tail of the target for laser initialization and electron beam diagnostics, respectively. See more details in Supplemental Material [26,27].

The laser pulses can stably beat inside the channel and drive the SP as shown in Figs. 1(a) and 1(b), where the structure of the wakefield is capable of accelerating both positively and negatively charged particles. The longitudinal wakefield E_z of amplitude 0.5 TV/m can be resonantly generated inside the vacuum channel, which accelerates totally 0.2 nC electrons to an energy of up to 10 MeV over a 40 μm interaction length, as shown in Fig. 1(c). This indicates an averaged peak acceleration gradient of $G_{\rm peak} \approx 0.25$ TeV/m. The normalized emittance of the full beam is $\varepsilon_{\rm N} = 0.12$ mm mrad and the rms beam divergence is $\sigma_\theta = 0.23$ rad. While these electrons are confined and accelerated on the surface, the majority of them can propagate longitudinally from the channel due to the strong E_z field. There is also a small fraction of electrons, e.g., about 20 fC from this simulation, which can escape transversely from the surface to be trapped during the laser scattering with the vertical edge of the microtube [9] and accelerated by the wakefield inside the vacuum channel to produce a narrow energy spectrum as shown in Fig. 1(g). The energy spectrum is peaked at 0.8 MeV, which indicates the mean acceleration gradient of $G_{\mathrm{mean}} \simeq 20$ GeV/m. The beam is well collimated with $\epsilon_{\mathrm{N}} = 43.2$ μm mrad and $\sigma_\theta = 12.5$ mrad. This is a general picture of the beating wave drive SP and its wakefield acceleration.

SP-based wakefield excitation can be understood as a stimulated Raman scattering process [28]. At the same time, the beat wave-driven SP is not identical to conventional bulk stimulated Raman scattering. This interaction can be self-consistently described using Maxwell's equations coupled to the cold-fluid model for the plasma electrons, formulated in cylindrical coordinates (r, ϕ, z). Inside the vacuum channel, $0 \le r < a$, the permittivity is $\epsilon_v = 1$. In the plasma wall, $r \ge a$, $\epsilon_p(\omega) = 1 - \omega_p^2/\gamma_0\omega^2$, where $\omega_p^2 = 4\pi n_0 e^2/m_e$. n_0 is the equilibrium density of cold electron plasma. γ_0 is an effective quiver-averaged relativistic mass factor. Here, we seek axisymmetric modes with a predominantly longitudinal accelerating field. The possible mode is the fundamental transverse magnetic (TM) mode, TM_0, which can be driven by ponderomotive [9] or space charge force [13]. The electromagnetic fields can be written as $\boldsymbol{E} = (E_r, 0, E_z)$ and $\boldsymbol{B} = (0, B_\phi, 0)$.

For the TM_0 mode with $e^{i(kz-\omega t)}$ dependence, the eigenwave equation for E_z is given as [8]

$$\left[\frac{\partial^2}{\partial r^2} + \frac{1}{r}\frac{\partial}{\partial r} + \epsilon_j \frac{\omega^2}{c^2} - k^2\right] E_z^{(j)} = 0, \tag{1}$$

where j denotes v or p, representing the equation in vacuum or plasma. k and ω represent the propagation constant and oscillation frequency of the mode, respectively. Therefore, we can define the radial evanescent constants as $\kappa_v = \sqrt{k^2 - \omega^2/c^2}$ and $\kappa_p = \sqrt{k^2 - \epsilon_p(\omega)\omega^2/c^2}$. The solution is given inside the vacuum as $E_z^{(v)}(r, z, t) = A_v I_0(\kappa_v r) e^{i(kz-\omega t)} + \mathrm{c.c.}$ and inside the plasma as $E_z^{(p)}(r, z, t) = A_p K_0(\kappa_p r) e^{i(kz-\omega t)} + \mathrm{c.c.}$, where I_0 and K_0 are modified Bessel functions of first and second kinds, respectively. A_v is a constant and $A_p = A_v I_0(\kappa_v a)/K_0(\kappa_p a)$. The radial electric field $E_r^{(j)}$ and azimuthal magnetic field $B_\phi^{(j)}$ are given as $E_r^{(j)} = -(ik/\kappa_j^2) dE_z^{(j)}/dr$ and $B_\phi^{(j)} = -(i\omega\epsilon_j/c\kappa_j^2) dE_z^{(j)}/dr$.

The dispersion function is defined by considering the boundary conditions at the interface $r = a$, where tangential E_z and B_ϕ are continuous as $E_z^{(v)}(a) = E_z^{(p)}(a)$ and $B_\phi^{(v)}(a) = B_\phi^{(p)}(a)$, given by

$$\mathcal{D}(\omega, k) = \frac{\epsilon_v}{\kappa_v}\frac{I_1(\kappa_v a)}{I_0(\kappa_v a)} + \frac{\epsilon_p}{\kappa_p}\frac{K_1(\kappa_p a)}{K_0(\kappa_p a)}, \tag{2}$$

where the eigenmode satisfies $\mathcal{D}(\omega, k) = 0$. The phase velocity is $v_{\mathrm{ph}} = \omega/k$ and group velocity $v_g = -(\partial\mathcal{D}/\partial k)/(\partial\mathcal{D}/\partial\omega)$. In the large-radius limit $ka \gg 1$ or, more precisely, $\kappa_j^{-1} \ll a$, the dispersion in Eq. (2) recovers to that on a planar surface with a curvature correction in order of $\mathcal{O}(1/a)$. The phase velocity is shown in Fig. 2, where this curvature correction leads to the divergence for different plasma densities. A smaller value of a moves the cylindrical SP dispersion further from the planar limit and, therefore, modifies the radial leakage of E_z into the vacuum channel. In contrast, all v_{ph}/c collapse onto the same curve on planar surfaces. This is the fundamental reason for the advantage of curved surfaces, as will be discussed later. Generally, in the vicinity of the SP resonance, $\omega/\omega_p \to 1/\sqrt{2\gamma_0}$, the wave number diverges $k \to \infty$, while both v_{ph} and v_{g} vanish as $v_{\mathrm{ph}} \to 0$ and $v_g \to 0$, corresponding to a standing wave strongly localized at the plasma-vacuum interface. In contrast, for $\omega/\omega_p \ll 1$, the dispersion approaches the light line, with $v_{\mathrm{ph}} \approx v_g \approx c$, which indicates a weakly bound SP. Notably, on a cylindrical interface, the phase velocity remains significantly higher near the resonant line than in the planar case due to curvature effects. This enhancement is particularly pronounced for lower plasma densities and therefore allows the resonant SP excitation at a near-critical-density plasma for relativistic particle acceleration.

A physical SP field depends on the specific drive for the eigenwave equation in Eq. (1). Let us consider two co-propagating linearly polarized laser pulses of sufficiently long duration as $\boldsymbol{a}_L(r,z,t) = \Re\{\boldsymbol{e}_\perp a_{0,1} f_1(r) e^{i(k_1 z - \omega_1 t)} + \boldsymbol{e}_\perp a_{0,2} f_2(r,t) e^{i(k_2 z - \omega_2 t)}\}$, where $f_l(r)$ is the laser transverse profile and $a_{0,l}$ is the amplitude of normalized vector potential with l denoting either 1 or 2 for the first and second laser pulses, respectively. Here, we consider two laser pulses of the same profiles as $f_l(r) = f(r)$, which does not

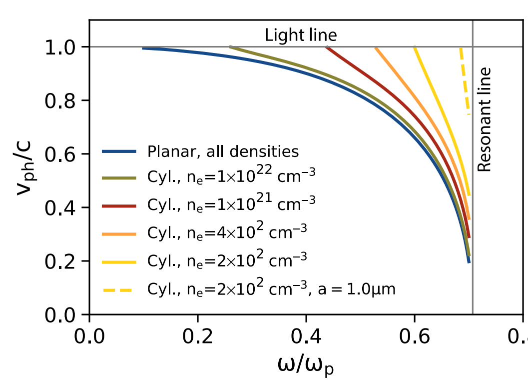

FIG. 2. Phase velocity v_{ph} of SP on planar and cylindrical surfaces of different plasma density, calculated with $a = 1.5$ μm by Eq. (2), except yellow dashed line with $a = 1.0$ μm.

introduce any new physics. The frequencies and wave numbers satisfy $\omega_l \simeq ck_l$ in vacuum. They create a slowly varying beating intensity of the time-averaged squared amplitude $\langle a_L^2(r,z,t)\rangle = a_{0,1}^2 f^2(r) + a_{0,2}^2 f^2(r) + 2|a_{0,1}||a_{0,2}| f^2(r)\cos(\Delta kz - \Delta\omega t)$ with $\Delta k = k_2 - k_1 > 0$ and $\Delta\omega = \omega_2 - \omega_1 > 0$. The cycle-averaged ponderomotive potential for electrons near the surface is given by $U_p(z,t) \simeq m_e c^2 \langle a_L^2(r,z,t)\rangle/4$. The beat ponderomotive force on electrons is $\boldsymbol{F}_p^{\text{beat}} = -\nabla U_p = F_{p,r}^{\text{beat}}\boldsymbol{e}_r + F_{p,z}^{\text{beat}}\boldsymbol{e}_z$, where the longitudinal and transverse components are given by $F_{p,z}^{\text{beat}}(z,t) = [m_e c^2 a_{0,1}a_{0,2}\Delta k f^2(a)\sin(\Delta kz - \Delta\omega t)]/2$, and $F_{p,r}^{\text{beat}}(z,t) = [2m_e c^2 a_{0,1}a_{0,2} a f^2(a)\cos(\Delta kz - \Delta\omega t)]/w_0^2$, respectively. For a solid surface and an optical laser beam where $\omega_p w_0/c \gg 1$, $F_{p,z}^{\text{beat}}$ dominantly modulates the surface electron density and current at the beat frequency and wave number $(\Delta\omega, \Delta k)$. Instead, $F_{p,r}^{\text{beat}}$ only creates the necessary charge separation across the vacuum-plasma interface to excite the surface mode. The feature is highly beneficial for maintaining the stability of the interface. See more details in the End Matter.

The physical field can be written as $\boldsymbol{E}^{sp}(r,z,t) = \Re\{\boldsymbol{\mathcal{E}}^{(j)}(r)A(z,t)\}$, where $A(z,t)$ contains the beat-wave phase. $\boldsymbol{\mathcal{E}}$ is the normalized eigenmode profile along $\hat{z}$ direction as $\boldsymbol{\mathcal{E}} = \boldsymbol{E}/\sqrt{\mathcal{N}_{sp}}$, where $\mathcal{N}_{sp}$ is the mode energy as $\mathcal{N}_{sp} = \sum_{j=v,p}\int_j d^2r_\perp[|\boldsymbol{B}|^2 + |\boldsymbol{E}|^2\partial_\omega(\omega\epsilon_j)]/16\pi$ with $\int d^2r_\perp$ denoting the integration over the cross-section transverse to z direction. Projecting the Maxwell equations onto the eigenmode yields a driven, damped oscillator for $A(z,t)$ as

$$\left(\frac{\partial^2}{\partial t^2} + 2\Gamma\frac{\partial}{\partial t} + \Omega_0^2 - \beta_{sp}\frac{\partial^2}{\partial z^2}\right)A(z,t) = S_{sp}a_{0,1}a_{0,2}\Delta k e^{i(\Delta kz - \Delta\omega t)}, \tag{3}$$

where $\Omega_0^2 = \omega_{sp}^2 - \beta_{sp}k_{sp}^2$ with $\beta_{sp} = \omega_{sp}v_g/k_{sp}$. Γ is the envelope damping rate. ω_{sp} and k_{sp} are the eigenfrequency and wave number and satisfy the dispersion relation in Eq. (2). S_{sp} is a coupling coefficient that depends on the overlap between the laser ponderomotive source and the SP eigenmode. After converting the longitudinal ponderomotive force into the associated beat current and factoring out $a_{0,1}a_{0,2}\Delta k$, it is calculated as $S_{sp} \simeq -(i\pi e n_0 c^2/2\gamma_0\omega_{sp}^2)\int_a^\infty r dr \mathcal{E}_z^*(r) f^2(r)$, where the radial contribution is neglected. See more details in Supplemental Material [26] and its included Ref. [27].

For a monochromatic near-resonant drive with slowly varying amplitude, the steady-state solution is approximately

$$A(z,t) \approx \frac{S_{sp}a_{0,1}a_{0,2}\Delta k}{\Omega_0^2 + \beta_{sp}\Delta k^2 - \Delta\omega^2 - 2i\Gamma\Delta\omega}e^{i(\Delta kz - \Delta\omega t)}. \tag{4}$$

The peak amplitude is then scaled as $E_{z,\max}^{\text{wake}} \approx G_{sp}a_{0,1}a_{0,2}E_{sp,0}$, where the natural SP field scale is defined by $E_{sp,0} = m_e c\omega_{sp}/e$. The dimensionless geometric factor G_{sp} measures how efficiently the beat ponderomotive force deposits energy into the normalized SP mode, and is defined by

$$G_{sp} \equiv \frac{|\mathcal{E}_z(a)|}{E_{sp,0}}\frac{|S_{sp}|\Delta k}{\mathcal{D}_{\text{eff}}}, \tag{5}$$

where $\mathcal{D}_{\text{eff}} = \sqrt{(\Omega_0^2 + \beta_{sp}\Delta k^2 - \Delta\omega^2)^2 + (2\Gamma\Delta\omega)^2}$. The detuning can be defined as $\delta_{sp} = \Delta\omega - \omega_{sp}(\Delta k)$, which is simplified to $\delta_{sp} \simeq \Delta\omega - \omega_{sp} - v_g(\Delta k - k_{sp})$ near the resonance. It is easy to see that G_{sp} carries geometry information, damping, and dispersion and depends on the material properties. G_{sp} is large if (1) $|\mathcal{E}_z(a)|$ is large (e.g., strong surface localization), (2) $|S_{sp}|$ is large (e.g., laser beam is well matched to mode radial structure), (3) detuning is small (e.g., the beam matches the SP dispersion), and (4) Γ is small (e.g., modest damping). The analytical solution of the SP field agrees well with the PIC simulation, as shown in Figs. 1(e) and 1(f), where a dimensionless normalized detuning $\varrho = \delta_{sp}/\omega_{sp} = 0.05$ is used for the lineout comparison. This value accounts for the small mismatch between the cold-fluid and the effective resonances observed in PIC, caused by finite-density evolution and relativistic corrections.

The resonance condition in Eq. (4) is $\omega_{sp}^2 + \beta_{sp}(\Delta k^2 - k_{sp}^2) - \Delta\omega^2 \approx 0$ for weak damping. The exact resonance occurs when $\Delta\omega = \omega_{sp}$ and $\Delta k = k_{sp}$. The cylindrical resonant condition is then obtained by satisfying the dispersion relation in Eq. (2) as $\mathcal{D}(\Delta\omega, \Delta k; n_e) = 0$. This means to choose a matched plasma density such that the cylindrical SP intersects the light line exactly at the beat frequency. If the radial decay of the SP field length in the core is much larger than the tube radius, as shown in Fig. 3(b), we have $\lim_{\kappa_v a\to 0} I_1(\kappa_v a)/[\kappa_v I_0(\kappa_v a)] = a/2$. As a result, the cylindrical resonant condition can be reduced to

$$\frac{1}{2} + \frac{\epsilon_p(\Delta\omega)}{\zeta}\frac{K_1(\zeta)}{K_0(\zeta)} = 0, \tag{6}$$

where $\zeta = \omega_p a/\sqrt{\gamma_0}c$. The resonant condition is numerically calculated and shown in Fig. 3(a). It is seen that for a finite density, the SP mode lives around $\omega \sim \mathcal{O}(\omega_p)$, and does not extend down to arbitrarily small ω on the light line where $\Delta\omega \to 0$. This implies that a single on-axis laser cannot resonantly excite a finite-frequency SP without additional asymmetry. The most efficient excitation occurs when the cylindrical SP mode admits v_{ph} close to c, while the field enhancement benefits from approaching the bound regime near the resonant line. The curvature allows the SP to be significantly faster than in the planar case at a similar

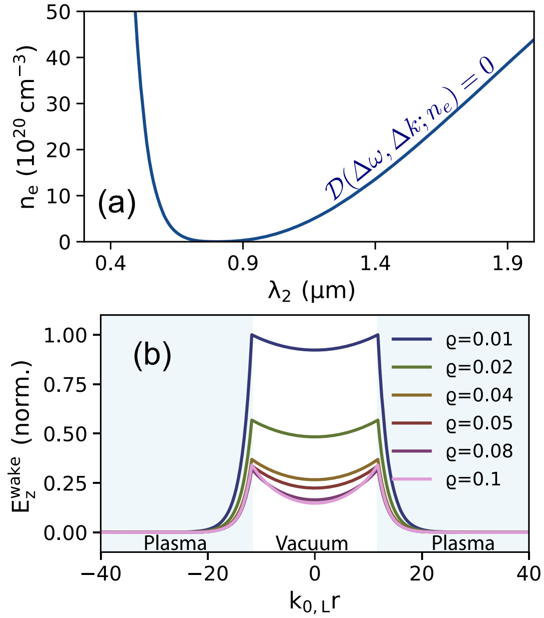

FIG. 3. (a) Resonant condition between matched plasma density n_e and second laser wavelength λ_2, where $\lambda_1 = 0.8$ μm, $a = 1.5$ μm, and $\gamma_0 = 1.0$, calculated by Eq. (6). (b) Radial distribution of $E_z^{\rm wake}$ for different values of normalized detuning ϱ. Here, $\Gamma = 0$. The light blue regions indicate the plasma wall.

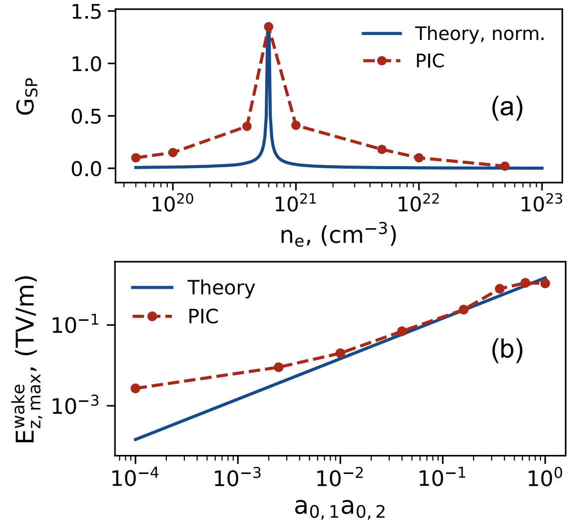

FIG. 4. (a) G_{sp} as a function of plasma density n_e from theory (normalized, blue solid) and PICs (red dot). (b) Amplitude of on-axis acceleration field $E_{z,\max}^{\rm wake}$ as a function of $a_{0,1}a_{0,2}$ from theory (blue solid) and PICs (red dot). Here, $a_{0,1} = a_{0,2} = a_0$. The other parameters are $\lambda_1 = 0.8$ μm, $\lambda_2 = 0.6$ μm, $a = 1.0$ μm, and $w_0 = 2.0$ μm. In (a), $a_0 = 0.6$, corresponding to laser peak powers $P_{1,\rm peak} = 48$ GW and $P_{2,\rm peak} = 80$ GW, respectively. In (b), $n_e = 6 \times 10^{20}$ cm^{-3}, close to the resonant density. The PIC results are obtained after the laser pulses copropagate 40 μm inside a microtube.

density. Equation (6) implies a $v_{\rm ph}$ close to c while staying in a near-critical regime, especially for large curvature, as shown in Fig. 2. This curvature effect is the key advantage of the cylindrical surface.

Equation (6) is a joint condition on the lasers and the plasma dispersion and geometry, with a trade-off controlled by detuning and damping. The field amplitude is significantly limited by detuning on a cold plasma surface, as shown in Fig. 3(b). By linearizing the dispersion around (ω_{sp}, k_{sp}) near the resonance, we have $\omega^2 \approx \omega_{sp}^2 + 2\omega_{sp}\delta\omega$ and $k^2 \approx k_{sp}^2 + 2k_{sp}\delta k$ with $\delta\omega = \Delta\omega - \omega_{sp}$ and $\delta k = \Delta k - k_{sp}$. The effective damping is reduced to $\mathcal{D}_{\rm eff}^{\rm res} \simeq 2\omega_{sp}\sqrt{(\delta\omega - v_g\delta k)^2 + \Gamma^2} \simeq 2\omega_{sp}\Gamma$. This will be a major experimental concern due to the inevitable laser-plasma mismatch in a real experiment.

In PIC simulations, G_{sp} can be simply calculated by $G_{sp}^{\rm PIC} = E_{z,\max}^{\rm wake}/(a_{0,1}a_{0,2}E_{sp,0})$ and presents the resonant enhancement, which agrees well with the theory, as shown in Fig. 4(a). The amplitude of acceleration field scales with $a_{0,1}a_{0,2}$, as shown in Fig. 4(b), which agrees with the theoretical scaling when $a_{0,1} = a_{0,2} = a_0 \geq 0.01$. This value $a_0 = 0.01$ corresponds to a 13.4 MW peak power for $\lambda_1 = 0.8$ μm and a 23.9 MW for $\lambda_2 = 0.6$ μm while the resonantly driven acceleration field reaches the GV/m level. This indicates that resonant SP excitation enables low-power lasers to act as effective drivers for strong wakefield generation. It can also be seen that SP growth is much faster in the ultralow-power regime, $a_0 < 0.01$, due to the small detuning rate caused by the weak surface density perturbation.

SP excitation occurs as soon as the outermost electrons of the surface material can be ionized by the laser field. For example, on a metallic crystalline surface, such as VCNT, laser pulses with a peak power of order 10 MW are sufficient to ionize the first π-bond electrons, thereby initiating SP resonant growth. However, at such low intensities, the resulting SP field remains too weak to trap electrons. Current PIC simulations in Fig. 4(b) indicate that efficient electron trapping occurs for $a_0 > 0.2$, corresponding to a laser power threshold of approximately 4 GW. Importantly, this power level lies well within the capabilities of currently available high-power fiber laser systems [19], demonstrating the experimental feasibility of resonant SP-driven wakefield acceleration.

In summary, the theory of resonant SP excitation driven by beating lasers presented in this Letter can be readily generalized to other drivers, including the Lorentz or ponderomotive force of a laser field and the space-charge force of a charged-particle beam. In each case, Eq. (3) is modified by the appropriate source term, and the corresponding eigenmodes become dominant depending on the coupling efficiency. Geometric effects can be treated similarly, and the efficiency can be improved by using structured drivers, such as Laguerre-Gaussian lasers. While this scheme works with lasers of a wide range of power from megawatts to petawatts, a particularly attractive prospect is to accelerate an electron beam up to a few MeV inside a solid microtube using portable GW lasers over a distance of tens of micrometres, while retaining substantial flexibility in energy spectrum, brightness, and beam size. Technically, this could be realized by attaching an ultrathin film to the output of standard laser optics. Such films can be fabricated with existing techniques using VCNT with well-structured channels. Experimentally, submicrometer transverse positioning and angular control at approximately the few-to-10 mrad level are desirable for maintaining predominantly axisymmetric TM_0 mode excitation. Such an alignment is challenging because of the micrometre-scale target geometry, but it is not fundamentally prohibitive [29]. Therefore, this beat-wave-driven scheme provides a compact and experimentally accessible path toward SP-based microscale accelerators and radiation sources for applications in ultrafast science, materials studies, and biomedical radiation technologies.

Acknowledgments—This work has been supported by the Science and Technology Facilities Council (STFC) through the Cockcroft Institute core grant UKRI1887. G. X. acknowledges the support from the Cockcroft Institute Core Grant No. ST/V001612/1. J. R.-L. acknowledges support by the Generalitat Valenciana under grant agreement CIDEGENT/2019/058. B. L. acknowledges the support of Guangdong Basic and Applied Basic Research Foundation (Grant No. 2025A1515011532) and Guangdong Major Talent Project (Grant No. 2023CX10Y036). This work made use of the Barkla High Performance Computing facilities at the University of Liverpool.

Data availability—The data that support the findings of this article are not publicly available upon publication because it is not technically feasible and/or the cost of preparing, depositing, and hosting the data would be prohibitive within the terms of this research project. The data are available from the authors upon reasonable request.

[1] R. H. Ritchie, Plasma losses by fast electrons in thin films, Phys. Rev. **106**, 874 (1957).

[2] R. W. Wood, XLII. On a remarkable case of uneven distribution of light in a diffraction grating spectrum, Philos. Mag. **4**, 396 (1902).

[3] U. Fano, The theory of anomalous diffraction gratings and of quasi-stationary waves on metallic surfaces (Sommerfeld's waves), J. Opt. Soc. Am. **31**, 213 (1941).

[4] A. Otto, Excitation of nonradiative surface plasma waves in silver by the method of frustrated total reflection, Z. Phys. A **216**, 398 (1968).

[5] X. F. Shen, A. Pukhov, and B. Qiao, Monoenergetic high-energy ion source via femtosecond laser interacting with a microtape, Phys. Rev. X **11**, 041002 (2021).

[6] J. Sarma, A. McIlvenny, N. Das, M. Borghesi, and A. Macchi, Surface plasmon-driven electron and proton acceleration without grating coupling, New J. Phys. **24**, 073023 (2022).

[7] A. McCay, A. McIlvenny, A. Macchi, L. Romagnani, P. Martin, O. Cavanagh, D. P. Molloy, L. Lancia, T. Dzelzainis, H. Ahmed, J. Sarma, S. Kar, D. Margarone, and M. Borghesi, Surface wave electron acceleration from flat foils at parallel laser incidence, Phys. Rev. Lett. **135**, 145001 (2025).

[8] B. Lei, H. Zhang, D. Seipt, A. Bonatto, B. Qiao, J. Resta-López, G. Xia, and C. Welsch, Coherent synchrotron radiation by excitation of surface plasmon polariton on near-critical solid microtube surface, Phys. Rev. Lett. **135**, 205001 (2025).

[9] B. Lei, H. Zhang, C. Bonţoiu, A. Bonatto, P. Martín-Luna, B. Liu, J. Resta López, G. Xia, and C. Welsch, Leaky surface plasmon-based wakefield acceleration in nanostructured carbon nanotubes, Plasma Phys. Controlled Fusion **67**, 065036 (2025).

[10] G. I. Stegeman, R. F. Wallis, and A. A. Maradudin, Excitation of surface polaritons by end-fire coupling, Opt. Lett. **8**, 386 (1983).

[11] L. Fedeli, A. Sgattoni, G. Cantono, D. Garzella, F. Réau, I. Prencipe, M. Passoni, M. Raynaud, M. Květoň, J. Proska, A. Macchi, and T. Ceccotti, Electron acceleration by relativistic surface plasmons in laser-grating interaction, Phys. Rev. Lett. **116**, 015001 (2016).

[12] A. A. Sahai, Nanomaterials based nanoplasmonic accelerators and light-sources driven by particle-beams, IEEE Access **9**, 54831 (2021).

[13] B. Lei, H. Zhang, C. Bonţoiu, A. Bonatto, J. Resta-López, G. Xia, B. Qiao, and C. Welsch, 100 s TeV/m-level particle accelerators driven by high-density electron beams in micro structured carbon nanotube forest channel, New J. Phys. **27**, 084301 (2025).

[14] C. Bonţoiu, A. Bonatto, Ö. Apsimon, L. Bandiera, G. Cavoto, I. Drebot, G. Gatti, J. Giner-Navarro, B. Lei, P. Martín-Luna, I. Rago, J. Rodríguez Pérez, B. S. Nunes, A. Sytov, C. Valagiannopoulos, C. P. Welsch, G. Xia, J. Zhang, and J. Resta-López, Numerical study of self-injected electron acceleration in CNT structured targets driven by an 800 nm laser, Sci. Rep. **15**, 45323 (2025).

[15] T. Tajima and M. Cavenago, Crystal x-ray accelerator, Phys. Rev. Lett. **59**, 1440 (1987).

[16] X. Zhang, T. Tajima, D. Farinella, Y. Shin, G. Mourou, J. Wheeler, P. Taborek, P. Chen, F. Dollar, and B. Shen, Particle-in-cell simulation of x-ray wakefield acceleration and betatron radiation in nanotubes, Phys. Rev. Accel. Beams **19**, 101004 (2016).

[17] M. Yu, H. H. Funke, J. L. Falconer, and R. D. Noble, High density, vertically-aligned carbon nanotube membranes, Nano Lett. **9**, 225 (2009).

[18] G. Aliana-Cervera, D. Mattia, C. Pasquino, R. Veness, and A. J. G. Lunt, Carbon nanotube wires for accelerator applications, Mater. Des. **258**, 114606 (2025).

[19] A. Lekosiotis, F. Belli, C. Brahms, M. Sabbah, H. Sakr, I. A. Davidson, F. Poletti, and J. C. Travers, On-target delivery of intense ultrafast laser pulses through hollow-core anti-resonant fibers, Opt. Express **31**, 30227 (2023).

[20] E. Esarey, C. B. Schroeder, and W. P. Leemans, Physics of laser-driven plasma-based electron accelerators, Rev. Mod. Phys. **81**, 1229 (2009).

[21] W. Horton and T. Tajima, Laser beat-wave accelerator and plasma noise, Phys. Rev. A **31**, 3937 (1985).

[22] Y. Kitagawa, T. Matsumoto, T. Minamihata, K. Sawai, K. Matsuo, K. Mima, K. Nishihara, H. Azechi, K. A. Tanaka, H. Takabe, and S. Nakai, Beat-wave excitation of plasma wave and observation of accelerated electrons, Phys. Rev. Lett. **68**, 48 (1992).

[23] A. Chamoli, D. N. Gupta, and V. Kumar, Surface plasma wave excitation using laser beat-wave and terahertz generation, Radiat. Eff. Defects Solids **179**, 962 (2024).

[24] D. Roa, J. Kuo, H. Moyses, P. Taborek, T. Tajima, G. Mourou, and F. Tamanoi, Fiber-optic based laser wakefield accelerated electron beams and potential applications in radiotherapy cancer treatments, Photonics **9**, 403 (2022).

[25] J. L. Vay, A. Almgren, J. Bell, L. Ge, D. P. Grote, M. Hogan, O. Kononenko, R. Lehe, A. Myers, C. Ng, J. Park, R. Ryne, O. Shapoval, M. Thévenet, and W. Zhang, Warp-X: A new exascale computing platform for beam–plasma simulations, Nucl. Instrum. Methods Phys. Res., Sect. A **909**, 476 (2018).

[26] See Supplemental Material at http://link.aps.org/supplemental/10.1103/2dkn-db5z for additional information on why longitudinal ponderomotive force dominates SP coupling, derivation of coupling coefficient, S_{sp}, practical estimation of geometric factor G_{sp}, curvature effect on dispersion relation, experimental alignment, and PIC simulation configurations, which includes Ref. [27].

[27] A. L. Falk, K.-C. Chiu, D. B. Farmer, Q. Cao, J. Tersoff, Y.-H. Lee, P. Avouris, and S.-J. Han, Coherent plasmon and phonon-plasmon resonances in carbon nanotubes, Phys. Rev. Lett. **118**, 257401 (2017).

[28] T. M. Antonsen and P. Mora, Self-focusing and Raman scattering of laser pulses in tenuous plasmas, Phys. Rev. Lett. **69**, 2204 (1992).

[29] Y. Gao, J. Bin, D. Haffa, C. Kreuzer, J. Hartmann, M. Speicher, F. H. Lindner, T. M. Ostermayr, P. Hilz, T. F. Rösch, S. Lehrack, F. Englbrecht, S. Seuferling, M. Gilljohann, H. Ding, W. Ma, K. Parodi, and J. Schreiber, An automated, 0.5 Hz nano-foil target positioning system for intense laser plasma experiments, High Power Laser Sci. Eng. **5**, e12 (2017).

End Matter

To quantitatively measure which component dominates the surface-plasmon excitation, let us define two coefficients,

$$C_z \equiv \int d^2 r_\perp \mathcal{E}_z^*(r) F_{p,z}^{\rm beat}, \quad \text{and} \quad C_r \equiv \int d^2 r_\perp \mathcal{E}_r^*(r) F_{p,r}^{\rm beat}. \tag{A1}$$

We now consider a strongly localized TM_0 mode with a thin skin depth $\delta_{\rm in} \ll a \le w_0$. Therefore, $\mathcal{E}_r$ and $\mathcal{E}_z$ can be roughly assumed to be constant across $\delta_{\rm in}$, evaluated at $r \approx a$. Together with the longitudinal and transverse beat force $(F_{p,z}^{\rm beat}, F_{p,r}^{\rm beat})$, integrating over the thin SP layer $r \in [a - \delta_{\rm in}, a]$ gives

$$C_z \sim 2\pi a \delta_{\rm in} E_z^*(a) \left[\frac{m_e c^2}{2} a_{0,1} a_{0,2} \Delta k f_1(a) f_2(a) \right], \tag{A2}$$

and

$$C_r \sim 2\pi a \delta_{\rm in} E_r^*(a) \left[\frac{m_e c^2}{2} a_{0,1} a_{0,2} \frac{4a}{w_0^2} f_1(a) f_2(a) \right], \tag{A3}$$

where $\boldsymbol{\mathcal{E}} = (\mathcal{E}_r, 0, \mathcal{E}_z)$ denotes the normalized TM_0 eigenfield. The ratio is calculated as

$$\left| \frac{C_r}{C_z} \right| \sim \left| \frac{E_r(a)}{E_z(a)} \right| \frac{4a}{\Delta k w_0^2}, \tag{A4}$$

where $|E_r/E_z| \sim \mathcal{O}(1)$ and $\Delta k \sim k_{sp} \gg w_0^{-1}$ near the resonance. Therefore,

$$\left| \frac{C_r}{C_z} \right| \sim 4 \frac{a}{w_0} \frac{1}{k_{sp} w_0} \ll 1, \tag{A5}$$

which means the contribution of the radial ponderomotive force to the SP drive is much smaller than that of the longitudinal beat force and can be neglected.